

## Interdiffusion across solid electrolyte-electrode interface

Jia-Mian Hu, Linyun Liang, Yanzhou Ji, Liang Hong, Kirk Gerdes, and Long-Qing Chen

Citation: [Applied Physics Letters](#) **104**, 213907 (2014); doi: 10.1063/1.4879835

View online: <http://dx.doi.org/10.1063/1.4879835>

View Table of Contents: <http://scitation.aip.org/content/aip/journal/apl/104/21?ver=pdfcov>

Published by the [AIP Publishing](#)

---

### Articles you may be interested in

[Microstructural coarsening effects on redox instability and mechanical damage in solid oxide fuel cell anodes](#)

J. Appl. Phys. **114**, 183519 (2013); 10.1063/1.4830015

[Evaluation of Sr<sub>2</sub>MMoO<sub>6</sub> \(M=Mg, Mn\) as anode materials in solid-oxide fuel cells: A neutron diffraction study](#)

J. Appl. Phys. **113**, 023511 (2013); 10.1063/1.4774764

[Redox instability, mechanical deformation, and heterogeneous damage accumulation in solid oxide fuel cell anodes](#)

J. Appl. Phys. **112**, 036102 (2012); 10.1063/1.4745038

[Predicting ionic conductivity of solid oxide fuel cell electrolyte from first principles](#)

J. Appl. Phys. **98**, 103513 (2005); 10.1063/1.2135889

[Electric conduction and dielectric relaxation processes in solid oxide fuel cell electrolyte La<sub>0.5</sub>Sr<sub>0.5</sub>Ga<sub>0.6</sub>Ti<sub>0.4</sub>O<sub>3</sub>](#)

J. Appl. Phys. **96**, 3889 (2004); 10.1063/1.1786675

---



**AIP** | Journal of  
Applied Physics

*Journal of Applied Physics* is pleased to  
announce **André Anders** as its new Editor-in-Chief

## Interdiffusion across solid electrolyte-electrode interface

Jia-Mian Hu,<sup>1,a),b)</sup> Linyun Liang,<sup>1,b)</sup> Yanzhou Ji,<sup>1</sup> Liang Hong,<sup>1</sup> Kirk Gerdes,<sup>2</sup> and Long-Qing Chen<sup>1</sup>

<sup>1</sup>Department of Materials Science and Engineering, The Pennsylvania State University, University Park, Pennsylvania 16802, USA

<sup>2</sup>National Energy Technology Laboratory, Morgantown, West Virginia 26507, USA

(Received 26 February 2014; accepted 14 May 2014; published online 30 May 2014)

A phase-field model is developed for studying the cation interdiffusion across electrolyte-electrode interfaces in solid oxide fuel cell (SOFC) that can be contributing to long timescale performance degradation. Demonstrated on an interface between an 8%molY<sub>2</sub>O<sub>3</sub>-stabilized ZrO<sub>2</sub> and a La<sub>0.65</sub>Sr<sub>0.3</sub>MnO<sub>3-x</sub> typically used in SOFC, time-dependent evolution of the cation interdiffusion profiles are predicted by linking the phase-field model to a diffusion equation. The simulated interdiffusion profiles agree with independent experimental data in both time and space domains at different temperatures. © 2014 AIP Publishing LLC. [<http://dx.doi.org/10.1063/1.4879835>]

Cation interdiffusion across solid phase interfaces occurs at all temperatures in multicomponent systems driven by chemical potential and electric potential gradients. Such interdiffusion is a primary contributor to performance degradation in many solid-state electrochemical devices.<sup>1,2</sup> In solid oxide fuel cells (SOFCs), ambipolar diffusion of multiple cations and oxygen anions occurs across the cathode-electrolyte interface through the migration of oxygen vacancy during cell fabrication and operation,<sup>3,4</sup> with impurity cations diffusing into the host crystal lattice. Such interdiffusion corrupts the ideal interface by introducing time-dependent changes to chemical compositions, which could affect electrochemical activity, interfacial free energy, and other fundamental properties. In a worse case, cation interdiffusion may promulgate formation of resistive phases at the interface and/or triple phase boundaries,<sup>4</sup> which significantly block the transport of oxygen anion and hence deteriorate the cell performance. Therefore, knowledge of cation interdiffusion is centrally important for designing SOFCs with improved durability.

Concentration profiles of cation interdiffusion can be measured experimentally for selected systems, but the vastness of the thermodynamic parameter space prohibits empirical analysis of every electrolyte-electrode system over relevant operating conditions and times. It is imperative, therefore, to computationally assess the time-dependent evolution of interdiffusion profiles across electrolyte-electrode interfaces, whereby promising materials systems and processing conditions can be identified. The theoretical interdiffusion behavior in one dimension can be described by a conventional diffusion equation<sup>5</sup>

$$\frac{\partial c(x,t)}{\partial t} = \frac{\partial}{\partial x} \left\{ \tilde{\mathbf{D}}[c(x,t)] \frac{\partial c(x,t)}{\partial x} \right\}, \quad (1)$$

where  $c$  is the concentration and  $x$  is the diffusion distance along the concentration gradient  $\partial c/\partial x$ . The concentration dependent interdiffusion matrix  $\tilde{\mathbf{D}}$  in Eq. (1) can in principle be extracted from experimentally measured concentration

profiles using Boltzmann-Matano analysis for a set of judiciously chosen diffusion couples with one common intersecting composition,<sup>6</sup> which however, is technically challenging for the present multicomponent electrode-electrolyte system.

This paper describes a phase-field description<sup>7</sup> developed to generate an effective interdiffusion matrix  $\tilde{\mathbf{D}}^{\text{eff}}$  in the electrolyte-electrode system of 8%molY<sub>2</sub>O<sub>3</sub>-stabilized ZrO<sub>2</sub> (YSZ) and La<sub>0.65</sub>Sr<sub>0.3</sub>MnO<sub>3-x</sub> (LSM) perovskite<sup>4</sup> typical in SOFCs. The 8%YSZ is tetragonal at room temperature and exhibits mixed cubic and tetragonal phases between approximately 600 °C and 2000 °C (Ref. 8), while the A-site deficient LSM herein is rhombohedral at both room temperature and higher temperatures.<sup>9</sup> A large amount of oxygen vacancies are present in both YSZ and LSM. The model assumes constant bulk interdiffusion matrices in single-phase YSZ electrolyte and LSM cathode, and institutes a scheme for combinatorial estimation of the matrix at the interface. Specifically, a phase variable  $\eta$  is introduced to represent these phases of different inter-diffusive behaviors, i.e.,  $\eta = 1$  and  $0$  for the single-phase YSZ and LSM, respectively, and  $0 < \eta < 1$  for their interface, as shown in Fig. 1(a). In doing so, the concentration-dependent interdiffusion matrix  $\tilde{\mathbf{D}}[c(x,t)]$  in Eq. (1) can be replaced by a phase variable-dependent effective interdiffusion matrix  $\tilde{\mathbf{D}}^{\text{eff}}[\eta(x,t)]$ . This is applicable because the evolution of  $\eta$  (via Allen-Cahn equation<sup>10</sup>) is linked to the evolution of the concentration profile. The simulated interdiffusion profiles are later shown to agree with high spatial resolution element concentration analysis via energy-dispersive spectrometry (EDS) equipped in transmission electron microscope (TEM)<sup>4</sup> in both time and space domains at different temperatures.

The analytical expression of the interdiffusion coefficient in single-phase YSZ or LSM is derived using early theories established for multicomponent diffusion in silicates<sup>11</sup> and ceramics.<sup>12</sup> For any of the six ions shown in Figure 1(a), the ionic flux  $J_i$  can be written as

$$J_i = u_i c_i \frac{\partial \mu_i}{\partial x} + e z_i c_i u_i \frac{\partial \phi}{\partial x} \quad (i = 1, 2 \dots 6), \quad (2)$$

<sup>a)</sup>E-mail: juh34@psu.edu

<sup>b)</sup>J.-M. Hu and L. Liang contributed equally to this work.

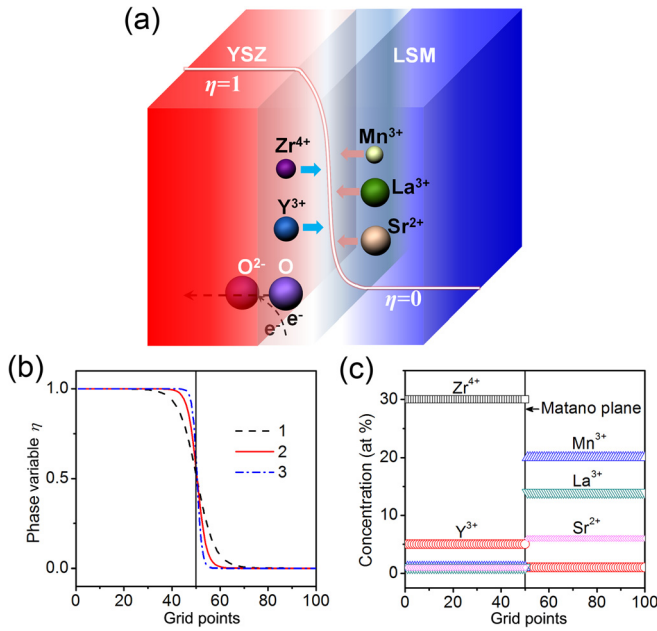


FIG. 1. (a) Schematics of the cation interdiffusion across the YSZ-LSM interface. The cationic and oxygen anionic fluxes are coupled by assuming zero flow of electric charges. (b) Interfaces of different width by taking  $W_0^* = 1, 4, 16$  for the interface “1,” “2,” “3,” respectively. (c) The initial concentration distribution across the interface.

where  $c_i$  and  $z_i$  are the concentration and valence of the ion, respectively;  $u_i$  is the mobility of the ion that relates to its tracer diffusion coefficient  $D_i^* = RTu_i$  ( $R$  is the ideal gas constant and  $T$  is the absolute temperature) via the Nernst-Einstein equation;<sup>13</sup>  $e$  is the elementary charge;  $\varphi$  is a mean electric potential relating to the average Coulomb force from the motion of all ions; the  $\partial\mu_i/\partial x$  and  $\partial\varphi/\partial x$  refer to the chemical potential gradient and electric potential gradient, respectively, which are the driving forces for the ionic fluxes. By assuming a zero net flow of electric charges

$$\sum_{i=1}^6 z_i J_i = 0, \quad (3)$$

and thereby the  $\partial\varphi/\partial x$  can be obtained as

$$e \frac{\partial\varphi}{\partial x} = \frac{\sum_{k=1}^6 z_k u_k c_k \frac{\partial\mu_k}{\partial x}}{\sum_{j=1}^6 z_j^2 u_j c_j}. \quad (4)$$

In light of Eq. (4),  $J_i$  can be further expressed as

$$J_i = u_i c_i \frac{\partial\mu_i}{\partial x} + u_i z_i c_i \frac{\sum_{k=1}^6 z_k u_k c_k \frac{\partial\mu_k}{\partial x}}{\sum_{j=1}^6 z_j^2 u_j c_j}. \quad (5)$$

Note that the condition of zero net charge flow [Eq. (3)] could also eliminate the flux of the oxygen anion<sup>14–16</sup> as a dependent variable and therefore focus on cationic flux. The chemical potential gradient  $\partial\mu_i/\partial x$  in Eq. (5) can further be

transformed into the measurable concentration gradient  $\partial c_i/\partial x$  based on

$$\begin{aligned} \mu_i &= \mu_i^0 + RT(\gamma_i c_i), \\ \partial\mu_i/\partial x &= RT \left( \frac{\partial \ln \gamma_i}{\partial x} + \frac{\partial c_i}{c_i \partial x} \right), \end{aligned} \quad (6)$$

where  $\mu_i^0$  is the chemical potential at the standard state and  $\gamma_i$  is the activity coefficient. Upon the local electroneutrality condition

$$\sum_{i=1}^6 z_i c_i = 0, \quad (7)$$

the concentration gradients of the five cations are intrinsically coupled as

$$\frac{\partial c_n}{\partial x} = - \sum_{k=1}^{n-1} (z_k/z_n) \frac{\partial c_k}{\partial x}. \quad (8)$$

Both solid electrolytes and electrodes are considered as near ideal solution ( $\gamma_i \approx 1$ ) for simplicity, with intrinsic diffusion coefficient almost equal to the tracer diffusion coefficient. Based on that, combination of Eqs. (5)–(8) yields the expressions for the cationic flux  $J_i$  and the interdiffusion tensor  $D_{ij}^s$  in the single-phase YSZ or LSM

$$\begin{aligned} J_i &= -D_{ij}^s \frac{\partial c_j}{\partial x} (i, j = 1, 2 \dots 5), \\ D_{ij}^s &= D_i^* \delta_{ij} - \left[ (D_i^* z_i z_j c_i) / \left( \sum_{k=1}^6 z_k^2 c_k D_k^* \right) \right] \\ &\quad \times (D_j^* - D_6^*) (i, j = 1, 2 \dots 5), \end{aligned} \quad (9)$$

where  $\delta_{ij} = 1$  and 0 for the diagonal ( $i = j$ ) and off-diagonal ( $i \neq j$ ) interdiffusion coefficients, respectively, and  $D_6^*$  denotes the tracer diffusion coefficient of the oxygen anion.

Furthermore, the effective interdiffusion matrix  $\tilde{D}_{ij}^{\text{eff}}$  across the YSZ-LSM interface is derived using a phase-field diffuse-interface description<sup>7</sup>

$$\tilde{D}_{ij}^{\text{eff}} = D_{ij}^{\text{YSZ}} h(\boldsymbol{\eta}) + D_{ij}^{\text{LSM}} [1 - h(\boldsymbol{\eta})], \quad (10)$$

where the  $D_{ij}^{\text{YSZ}}$  and  $D_{ij}^{\text{LSM}}$  are the constant interdiffusion matrix of single-phase YSZ and LSM and depend on the electric charges, concentrations, and tracer diffusion coefficients of all six ions via Eq. (9). An interpolating function  $h(\boldsymbol{\eta}) [= \boldsymbol{\eta}^3(6\boldsymbol{\eta}^2 - 15\boldsymbol{\eta} + 10)]$  is introduced to produce a linear combination of the  $D_{ij}^{\text{YSZ}}$  and  $D_{ij}^{\text{LSM}}$  at the YSZ-LSM interface ( $0 < \boldsymbol{\eta} < 1$ ). The function ensures  $h(\boldsymbol{\eta} = \mathbf{0}) = 0$  and  $h(\boldsymbol{\eta} = \mathbf{1}) = 1$ , and also that local energy minima existing at  $\boldsymbol{\eta} = \mathbf{0}$  and  $\mathbf{1}$  for subsequent free energy construction. Selection of a different interpolating function will certainly change the spatial distribution of  $\tilde{D}_{ij}^{\text{eff}}$  (and hence cations) at the interface, however, significant alterations to the obtained concentration profiles only occur when the magnitudes of  $D_{ij}^{\text{YSZ}}$  and  $D_{ij}^{\text{LSM}}$  are sufficiently different from each other, as discussed later. In light of Eq. (10), Eq. (1) can be rewritten as

$$\frac{\partial c_i}{\partial t} = \nabla \cdot \left\{ \tilde{D}_{ij}^{\text{eff}} [\eta(x, t)] \nabla c_j \right\} (i, j = 1, 2, \dots, 5). \quad (11)$$

Meanwhile, the temporal and spatial evolution of the non-conserved<sup>7</sup> phase variable  $\eta$  is described using the Allen-Cahn equation<sup>10</sup>

$$\frac{\partial \eta}{\partial t} = L \left[ W_0 \nabla^2 \eta - \frac{\partial f(c_i, \eta)}{\partial \eta} \right], \quad (12)$$

where  $L$  [ $\text{m}^3 \text{J}^{-1} \text{s}^{-1}$ ] is the kinetic evolution coefficient, and the  $f(c_i, \eta)$  is the chemical free energy of the LSM-YSZ composites, constructed as

$$\begin{aligned} f(c_i, \eta) = & \sum_{i=Y, Zr} \left[ (c_i - c_i^0)^2 h(\eta) + (c_i - 0)^2 (1 - h(\eta)) \right] \\ & + \sum_{i=Mn, La, Sr} \left[ (c_i - 0)^2 h(\eta) + (c_i - c_i^0)^2 (1 - h(\eta)) \right] \\ & + 2(\eta^4 - 2\eta^3 + \eta^2). \end{aligned} \quad (13)$$

From Eq. (13), evolution of  $\eta$  is related to the concentration  $c$ , thus allowing coupled evolution of  $\eta$  and  $c$ . The last term on the right of Eq. (13) is a double-well function which shows doubly degenerate minima at the bulk YSZ ( $\eta=1$ ) and LSM ( $\eta=0$ ) phases, but the concentration gradients in the composites would shift the minimum between them. Variations in the expression of the energy function  $f(c_i, \eta)$  may lead to changes in the width of the YSZ-LSM interface ( $W$ ). Moreover, the gradient energy coefficient  $W_0$  ( $\text{J m}^{-1}$ ) relates to the interface width as  $W \propto \sqrt{W_0}$  following diffuse-interface theory.<sup>17,18</sup> Shown in Fig. 1(b) are examples of YSZ-LSM interfaces with different width created by varying  $W_0$ , which would generate different distributions of the effective interdiffusion coefficient  $\tilde{D}_{ij}^{\text{eff}}$  across the interface. Utilizing these different spatial distributions of  $\tilde{D}_{ij}^{\text{eff}}$ , Eqs. (11) and (12) are solved iteratively using finite-difference method in a one-dimensional discretized

system of  $100\Delta x$ , with the grid size  $\Delta x = \Delta x^* \Delta l$ , where  $\Delta x^*$  is the reduced grid size and  $\Delta l$  is a characteristic length in real space. Nondimensionalization is also performed for the other coefficients in Eqs. (11) and (12) as

$$\Delta t^* = \frac{D_c \Delta t}{(\Delta l)^2}, \quad L^* = \frac{L f_c (\Delta l)^2}{D_c}, \quad W_0^* = \frac{W_0}{f_c (\Delta l)^2}, \quad f^* = \frac{f}{f_c}, \quad (14)$$

where  $D_c$  [ $\text{m}^2 \text{s}^{-1}$ ] and  $f_c$  [ $\text{J m}^{-3}$ ] are the scaling coefficients for the interdiffusion coefficients and free energy density, respectively. The initial concentration distributions of cations are uniform with  $c = c_i^0$  from  $n_x = 0$  to  $n_x = 50$ , and  $c \approx 0$  for  $n_x > 50$  for  $\text{Zr}^{4+}$  and  $\text{Y}^{3+}$  in the YSZ electrolyte. A similar arrangement is adopted for  $\text{Mn}^{3+}$ ,  $\text{La}^{3+}$ , and  $\text{Sr}^{2+}$  in the LSM electrode, as shown in Fig. 1(c), where  $n_x$  is the number of grid points. Values of  $c_i^0$  are calculated based on the bulk molecular formula. Note that the oxide interface investigated is within the frames of both the solvent-fixed and volume-fixed references,<sup>11,12</sup> where the matano plane fixing two equal areas on the concentration profiles<sup>5</sup> always locates at the center of the simulation system ( $n_x = 50$ ) due to the equal assumed molar volumes of the YSZ and LSM.

For illustration, we first simulate the cation interdiffusion profiles measured via high spatial resolution EDS in the electrolyte-electrode system of YSZ-LSM fabricated by co-firing at  $1400^\circ\text{C}$  for 60 min in an air furnace.<sup>4</sup> Taking  $\Delta x^* = 0.5$ ,  $\Delta l = 3 \text{ nm}$ , and  $\Delta t^* = 0.001$  for a real time step of  $\Delta t = 0.9 \text{ s}$ , the evolution of the cation interdiffusion profiles is illustrated in Figs. 2(a)–2(c) with  $W_0^* = 4$  [corresponding to the interface “2” in Fig. 1(b)]. The length of the interdiffusion zone (i.e.,  $W_L$ )<sup>19</sup> is about 30 nm after 12 min [Fig. 2(a)] and will continue expanding in the presence of a concentration gradient [Figs. 2(b) and 2(c)]. Of particular interest, the interdiffusion profiles after 60 min co-firing [Fig. 2(c)] in general agree with the experimental data in Ref. 4 [symbols in Fig. 2(c)], thus validating the model description of cation interdiffusion behavior across the solid electrolyte-electrode

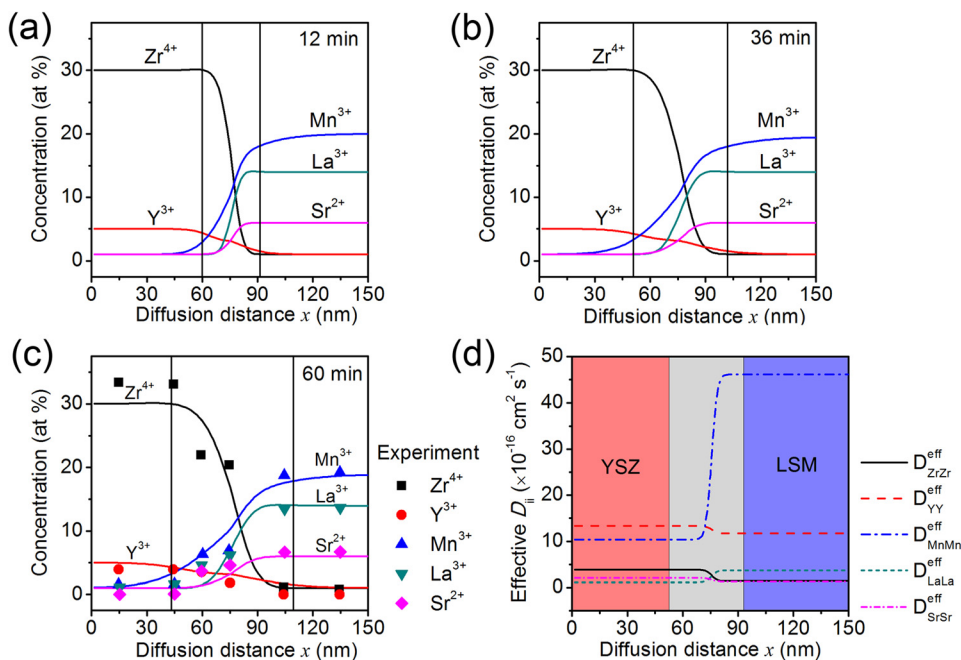


FIG. 2. Cation inter-diffusion profiles across the YSZ-LSM interface after co-firing at  $1400^\circ\text{C}$  for (a) 12 min, (b) 36 min, (c) 60 min, and corresponding experimental data (symbols). (d) Distributions of the diagonal values of the effective interdiffusion matrix across the interface (the central gray region) at 60 min.

interface. Discrepancies between experiments and simulations may arise from errors in measurements and/or simplifications in the model. For example, one key kinetic phenomenon ignored in the present model is cation loss to chemical sinks, such as the formation of secondary phases (e.g.,  $\text{La}_2\text{Zr}_2\text{O}_7$  or  $\text{SrZrO}_3$ , Ref. 4) at the interface under the high processing temperature of  $1400^\circ\text{C}$ . Concentration profiles for diffusion influenced by phase changes can be predicted,<sup>20</sup> but such is beyond the scope of the present interdiffusion model.

The tracer diffusion coefficients  $D_i^*$  of all cations and the oxygen anion at  $1400^\circ\text{C}$  with their bulk interdiffusion matrix  $D_{ij}^{\text{YSZ}}$  (or  $D_{ij}^{\text{LSM}}$ ) in single-phase YSZ (or LSM) calculated via Eq. (9) are listed in Table S1 in the Supplemental Materials.<sup>21</sup> Although the tracer diffusion coefficients used as input are obtained by calibrating the experimentally measured interdiffusion profiles across the LSM-YSZ interface (Ref. 4), they are comparable in magnitude to available data taken from tracer experiments<sup>22</sup> (e.g., the experimentally measured tracer diffusion coefficient of  $\text{Zr}^{4+}$  in YSZ is also at the order of  $10^{-16} \text{ cm}^2 \text{ s}^{-1}$  at  $1400^\circ\text{C}$ , see the first paper listed in Ref. 22) and/or *ab initio* calculations.<sup>23</sup> Note that the diagonal values of the interdiffusion matrix correspond to the intrinsic diffusion behavior of a certain cation while the off-diagonal values govern the strength of inter-coupling among different cationic fluxes. Specifically, the diagonal elements  $D_{\text{MnMn}}^{\text{YSZ}}$ ,  $D_{\text{LaLa}}^{\text{YSZ}}$ , and  $D_{\text{SrSr}}^{\text{YSZ}}$  are two orders of magnitude larger than the off-diagonal ones, indicating a weak inter-coupling for the cations of  $\text{Mn}^{3+}$ ,  $\text{La}^{3+}$ , and  $\text{Sr}^{2+}$  in the YSZ electrolyte. Accordingly, the interdiffusion profiles of these three cations [Figs. 2(a)–2(c)] demonstrate independence in their respective interdiffusion length along the YSZ-rich side [ $x < 75 \text{ nm}$ , on the left of the matano plane] compared to those in the LSM-rich side [ $x > 75 \text{ nm}$ , on the right of the matano plane]. Similarly, the  $\text{Zr}^{4+}$  and  $\text{Y}^{3+}$  cations show remarkably independent interdiffusion behaviors in the LSM electrode due to the much larger diagonal  $D_{\text{ZrZr}}^{\text{LSM}}$  and  $D_{\text{YY}}^{\text{LSM}}$ , and evidenced by distinctly unique interdiffusion lengths along the LSM-rich side. Detailed analysis on the interdiffusion length of each cation will be shown later.

Moreover, the differences between the single-phase interdiffusion matrices  $D_{ij}^{\text{YSZ}}$  and  $D_{ij}^{\text{LSM}}$  at  $1400^\circ\text{C}$  are in general not large (Table S1 in Ref. 21). As a result, the effective interdiffusion matrix  $\tilde{D}_{ij}^{\text{eff}}$  shows relatively small changes across the interface and therefore depends weakly on the distributions of the phase variable  $\eta$  [Eq. (10)]. For illustration, Figure 2(d) shows the spatial distributions of the diagonal values ( $i=j$ ) of  $\tilde{D}_{ij}^{\text{eff}}$  at 60 min, among which only the  $\text{Mn}^{3+}$  exhibits a distinct change of about  $35.81 \times 10^{-16} \text{ cm}^2 \text{ s}^{-1}$  across the interface. This accounts for the appreciably asymmetric behavior [see Fig. 2(c)] in the cation interdiffusion profiles of  $\text{Mn}^{3+}$  along the two sides of the matano plane, whereas profiles of the other cations are more symmetric. We further performed simulations using different interface configurations (distributions of  $\eta$ ) shown in Fig. 1(b), but the obtained interdiffusion profiles show little difference with those in Figs. 2(a)–2(c) (not shown here). Such is further evidence for the overall weak dependence of  $\tilde{D}_{ij}^{\text{eff}}$  on the distributions of  $\eta$  in the specific electrolyte-electrode system.

The above-mentioned YSZ-LSM sample was further annealed at  $1000^\circ\text{C}$  in an air furnace for another 1000 h.<sup>4</sup> For further validation, we simulated the time-dependent cation interdiffusion during such annealing process, using the concentration profiles obtained in Fig. 2(c) as the input. The temperature dependence of the tracer diffusion coefficient is given by the Arrhenius-type relation

$$D_T^* = D_{T_0}^* \exp \left[ \frac{Q}{k_B} \left( \frac{1}{T_0} - \frac{1}{T} \right) \right], \quad (15)$$

where  $T_0$  is the reference temperature (1673 K),  $D_{T_0}^*$  is the tracer diffusion coefficient at  $T_0$ ,  $Q$  is the activation energy, and  $k_B$  is the Boltzman constant.

Figures 3(a)–3(c) display the time-dependent cation interdiffusion profiles at  $1000^\circ\text{C}$ . Among them, the simulated profiles after a 1000 h annealing [solid lines in Fig. 3(c)] agree well with experimental measurements on the same sample<sup>4</sup> that is first co-fired at  $1400^\circ\text{C}$  for 1 h then annealed at  $1000^\circ\text{C}$  for 1000 h [the symbols in Fig. 3(c)].

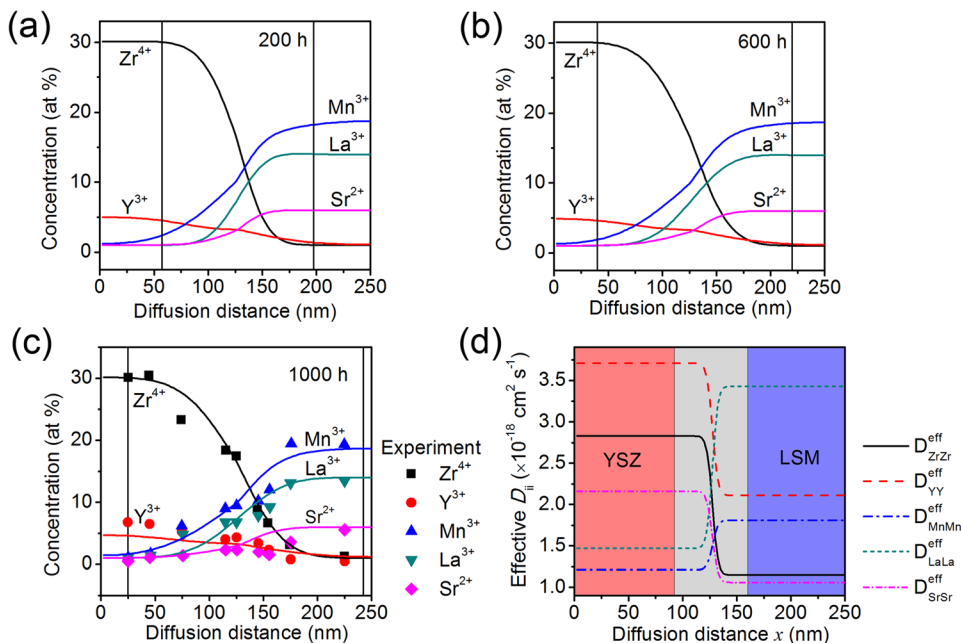


FIG. 3. Cation inter-diffusion profiles across the YSZ-LSM interface after prolonged annealing at  $1000^\circ\text{C}$  for (a) 200 h, (b) 600 h, (c) 1000 h, and corresponding experimental data (symbols). (d) Distributions of the diagonal values of the effective interdiffusion matrix across the interface (the central gray region) at 1000 h.

The values of the tracer diffusion coefficients  $D_i^*$ , the activation energy  $Q$ , and the single-phase interdiffusion matrices  $D_{ij}^{\text{YSZ}}$  and  $D_{ij}^{\text{LSM}}$  at 1000 °C calculated via Eq. (9) are summarized in Table S2 in Ref. 21. Similarly to the case at 1400 °C, the diagonal values of both  $D_{ij}^{\text{YSZ}}$  and  $D_{ij}^{\text{LSM}}$  are about two orders of magnitude larger than the off-diagonal values for the impurity cations (viz., the  $\text{Mn}^{3+}/\text{La}^{3+}/\text{Sr}^{2+}$  in YSZ and the  $\text{Zr}^{4+}/\text{Y}^{3+}$  in LSM). Accordingly, a weak inter-coupling among these ionic fluxes is exhibited. Figure 3(d) further shows the relative changes in the diagonal values of  $\tilde{D}_{ij}^{\text{eff}}$  (i.e.,  $\tilde{D}_{ii}^{\text{eff}}$ ) across the interface after annealing for 1000 h, in which larger  $\tilde{D}_{ii}^{\text{eff}}$  corresponds to faster interdiffusion with smaller slope in the concentration profiles. However, as the relative changes in  $\tilde{D}_{ii}^{\text{eff}}$  across the interface are much smaller than the case at 1400 °C [cf.  $\tilde{D}_{\text{MnMn}}^{\text{eff}}$  in Fig. 2(d)], the simulated concentration profiles are basically symmetric along the two sides of the matano plane.

Furthermore, as the average changes in the effective interdiffusion matrix  $\tilde{D}_{ij}^{\text{eff}}$  across the interface are not large at both 1400 °C and 1000 °C, the whole evolution can be approximated as two isothermal interdiffusion processes with constant  $\tilde{D}_{ij}^{\text{eff}}$ . In this regard, the length of interdiffusion zone for each ion ( $W_L$ ) should almost be in linear proportion to the square root of the time ( $t^{1/2}$ ),<sup>5</sup> as demonstrated in Fig. S1 in Ref. 21.

Finally, we would like to mention that the present model focuses on the ambipolar interdiffusion of cation(s)-oxygen anion pair(s) across the electrolyte-electrode interface during the high-temperature processing of SOFCs by assuming local charge neutrality condition [Eqs. (3) and (7)]. It should be pointed that the presence of electron conduction in LSM and oxygen vacancy diffusion in YSZ could reduce the ambipolar nature of cation interdiffusion between LSM and YSZ. It should also be noted that the possible diffusion along the electrolyte-electrode interface (i.e., interphase diffusion) at such high temperature (e.g., 1400 °C) is beyond the scope of this paper. Modification in electrostatic boundary conditions is required to predict the interdiffusion during the cell operation of SOFCs with the presence of electrode polarization.

In summary, the cation interdiffusion behaviors across the solid oxide interface of YSZ-LSM have been described based on a phase-field model derived for phase-variable-dependent effective interdiffusion matrix of multiple cations. The simulated interdiffusion profiles agree well with the experimental data in both time and space domains at two different temperatures (1400 °C and 1000 °C). The model provides a good starting point for investigation of the interdiffusion in the YSZ-LSM systems of different compositions and can be easily extended to other electrolyte-electrode

systems in SOFCs. The rather general concepts of ionic interdiffusion across the solid oxide interface are transferable to other solid-state electrochemical devices such as solid-state lithium batteries.<sup>24</sup>

This work was supported by the National Energy Technology Laboratory's on-going research in the area of cathode modeling in Solid Oxide Fuel Cells under the URS Contract No. 0004000.3.621.054.001.211.000.007.

- <sup>1</sup>H. Yokokawa, H. Tu, B. Iwanschitz, and A. Mai, *J. Power Sources* **182**, 400 (2008).
- <sup>2</sup>A. T. Duong and D. R. Mumm, *J. Power Sources* **241**, 281 (2013).
- <sup>3</sup>M. Palcut, R. Knibbe, K. Wiik, and T. Grande, *Solid State Ionics* **202**, 6 (2011).
- <sup>4</sup>C.-C. T. Yang, W.-C. J. Wei, and A. Roosen, *J. Am. Ceram. Soc.* **87**, 1110 (2004).
- <sup>5</sup>H. Schmalzried, *Solid State Reactions* (Verlag Chemie GmGH, Weinheim/Bergstr, Germany, 1974).
- <sup>6</sup>J. S. Kirkaldy, J. E. Lane, and G. R. Mason, *Can. J. Phys.* **41**, 2174 (1963).
- <sup>7</sup>L. Q. Chen, *Annu. Rev. Mater. Res.* **32**, 113 (2002).
- <sup>8</sup>H. G. Scott, *J. Mater. Sci.* **10**, 1527 (1975).
- <sup>9</sup>A. Hammouche, E. Siebert, and A. Hammou, *Mater. Res. Bull.* **24**, 367 (1989).
- <sup>10</sup>J. W. Cahn, *Acta Metall.* **9**, 795 (1961).
- <sup>11</sup>A. C. Lasaga, *Geochim. Cosmochim. Acta* **43**, 455 (1979).
- <sup>12</sup>A. R. Cooper, *Phys. Chem. Glasses* **6**, 55 (1965).
- <sup>13</sup>W. Jost, *Diffusion in Solids, Liquids, Gases* (Academic Press, New York, 1952).
- <sup>14</sup>T. Horita, K. Yamaji, N. Sakai, Y. Xiong, T. Kato, H. Yokokawa, and T. Kawada, *J. Power Sources* **106**, 224 (2002).
- <sup>15</sup>X.-M. Bai, Y. Zhang, and M. R. Tonks, *Phys. Chem. Chem. Phys.* **15**, 19438 (2013).
- <sup>16</sup>Y. L. Yang, A. J. Jacobson, C. L. Chen, G. P. Luo, K. D. Ross, and C. W. Chu, *Appl. Phys. Lett.* **79**, 776 (2001).
- <sup>17</sup>S. G. Kim, W. T. Kim, and T. Suzuki, *Phys. Rev. E* **60**, 7186 (1999).
- <sup>18</sup>M. Asle Zaeem, H. El Kadiri, S. Mesarovic, M. Horstemeyer, and P. Wang, *J. Phase Equilib. Diffus.* **32**, 302 (2011).
- <sup>19</sup>For simplicity, we use the interdiffusion profile of  $\text{Zr}^{4+}$  as a criterion to define the length of the interdiffusion zone  $W_L$  unless specified otherwise. Detailed analyses on the zone length of other cations are shown in Fig. S1 of Ref. 21.
- <sup>20</sup>T. W. Heo, S. Bhattacharyya, and L.-Q. Chen, *Philos. Mag.* **93**, 1468 (2012).
- <sup>21</sup>See supplementary material at <http://dx.doi.org/10.1063/1.4879835> for the values of the input parameters mentioned in the main text and the time-dependent interdiffusion zone length for all five cations at two different temperatures.
- <sup>22</sup>M. Kilo, G. Borchardt, B. Lesage, O. Kaitasov, S. Weber, and S. Scherrer, *J. Eur. Ceram. Soc.* **20**, 2069 (2000); M. Kilo, M. A. Taylor, C. Argirusis, G. Borchardt, B. Lesage, S. Weber, S. Scherrer, H. Scherrer, M. Schroeder, and M. Martin, *J. Appl. Phys.* **94**, 7547 (2003); M. Kilo, M. A. Taylor, C. Argirusis, G. Borchardt, S. Weber, H. Scherrer, and R. A. Jackson, *J. Chem. Phys.* **121**, 5482 (2004); S. Miyoshi and M. Martin, *Phys. Chem. Chem. Phys.* **11**, 3063 (2009).
- <sup>23</sup>M. Kilo, R. A. Jackson, and G. Borchardt, *Philos. Mag.* **83**, 3309 (2003).
- <sup>24</sup>K. Takada, *Acta Mater.* **61**, 759 (2013).